

Magnetic order in the repulsive Fermi-Hubbard model in three-dimensions and the crossover to two-dimensions

Jie Xu, Simone Chiesa, Eric J. Walter, Shiwei Zhang

Department of Physics, College of William and Mary, Williamsburg, VA 23187, USA

Systems of fermions described by the three-dimensional (3D) repulsive Hubbard model on a cubic lattice have recently attracted considerable attention due to their possible experimental realization via cold atoms in an optical lattice. Because analytical and numerical results are limited away from half-filling, we study the ground state of the doped system from weak to intermediate interaction strengths within the generalized Hartree-Fock approximation. The exact solution to the self-consistent-field equations in the thermodynamic limit is obtained and the ground state is shown to exhibit antiferromagnetic order and incommensurate spin-density waves (SDW). At low interaction strengths, the SDW has unidirectional character with a leading wave-vector along the $\langle 100 \rangle$ -direction, and the system is metallic. As the interaction increases, the system undergoes a simultaneous structural and metal-to-insulator transition to a unidirectional SDW state along the $\langle 111 \rangle$ -direction, with a different wavelength. We systematically determine the real- and momentum-space properties of these states. The crossover from 3D to two-dimensions (2D) is then studied by varying the inter-plane hopping amplitude, which can be experimentally realized by tuning the distance between a stack of square-lattice layers. Detailed comparisons are made between the exact numerical results and predictions from the pairing model, a variational *ansatz* based on the pairing of spins in the vicinity of the Fermi surface. Most of the numerical results can be understood quantitatively from the *ansatz*, which provides a simple picture for the nature of the SDW states.

PACS numbers: 75.30.Fv, 71.15.Ap, 71.45.Lr, 71.10.Fd, 75.10.Lp, 75.50.Ee

I. INTRODUCTION

Over the past several years, optical lattices have become an increasingly powerful tool for emulating many systems in condensed matter physics¹⁻⁴. An optical lattice can provide exceptionally clean access to a variety of model many-body Hamiltonians in which parameters can be systematically tuned and controlled. Thus, they make possible quantitative experimental study of the properties of interacting electron models, which have proven extremely challenging for analytic and numerical approaches alone. The combination of these approaches presents unprecedented opportunities for improving our understanding of interacting electron systems, by testing theoretical concepts and increasing the accuracy and predictive power of numerical approaches via comparison with experiment.

The one-band Hubbard model is one of the most fundamental models in condensed matter physics. It has been widely studied in two dimensions (2D)⁵⁻²⁰ as the simplest model for the Cu-O plane in cuprate superconductors. For the three-dimensional (3D) Hubbard model, however, considerably less is known from both theoretical and experimental sides. Optical lattices play, in this respect, a particularly fundamental role as they allow for a clean experimental realization of the 3D model and offer the interesting possibility of tuning the hopping parameter along one direction, t_{\perp} , thereby allowing a systematic study of the evolution of properties as the system crosses over from 3D to 2D.

Thanks to advances in the ability to directly cool atoms in optical lattices²¹, experiments are nearing the realization of phases with magnetic order. It is thus particu-

larly important and timely to understand such phases in the Hubbard model. Somewhat surprisingly, apart from half-filling (one particle per site), which displays antiferromagnetic (AFM) order, the nature of the magnetic properties in the 3D Hubbard model has not been characterized, even at the mean-field level. In this work, we study the magnetic properties in the ground states of the 3D Hubbard model and in the crossover regime, using generalized Hartree-Fock (HF) theory. It is shown that the system has a tendency to form unidirectional spin-density wave (SDW) states with AFM order and a modulating wave along either the $\langle 100 \rangle$ - (at low U/t) or the $\langle 111 \rangle$ -direction (at higher U/t). We examine the evolution of the SDW wavelength in the full mean-field solution as U , density and t_{\perp} vary and characterize the ground state by its properties in real and momentum space.

Despite the simple nature of the mean-field approach, the determination of the correct equilibrium properties in these models is not straightforward^{20,22}. The main challenge lies in finding an unbiased strategy to determine the leading wave-vector(s) characterizing the spatial dependence of the order parameter. Calculations are performed in a real space simulation cell and most choices of the cell will return solutions that are biased by finite-size effects. This is often further complicated by shell effects and sensitivity of the solution to the topology of the Fermi surface, which often lead to local minimum solutions.

To overcome the difficulties, it is necessary to move to larger and larger cells and gain insights from the evolution of the corresponding solutions. This line of attack has become increasingly possible because of the dramatic

increase in computing power and continuous algorithmic progress. In the present work, we combine such an approach with more targeted searches to obtain the global minimum solution of the self-consistent-field (SCF) equations in the thermodynamic limit. Furthermore, we show how the numerical results can be understood by a variational ansatz based on the pairing of spins in the vicinity of the Fermi surface. Detailed comparisons are made between the direct numerical solutions and the pairing ansatz predictions. The excellent agreement helps to provide a simple, predictive picture for the properties of the SDW states.

The mean-field approach is often the starting point in the study of strongly interacting systems such as the Hubbard model. Although the approximations involved can lead to significant errors, mean-field theory often provides insights into qualitative aspects of the behavior of many-body systems. Moreover, comparisons with quantum Monte Carlo results¹⁹ have shown²⁰ that, in 2D, the mean-field solution captures the basic physics of SDW states at intermediate interaction strengths, and provides a good qualitative (or even quantitative in some aspects) description of the magnetic correlations in the true ground state. Because it is reasonable to expect a similar level of accuracy for the models presently considered, we expect that our findings will provide guidance to many-body approaches and experimental studies alike.

We have limited our study to $U \lesssim 6t$, where the mean-field approach can be expected to offer useful insight. Below we will discuss the mean-field predictions and their implications (and the caveats) on the true many-body states drawing from the comparison in 2D^{19,20}. Clearly, the form of generalized mean-field theory considered in this work will not capture exotic instabilities, such as unconventional pairing order. Indeed, as U increases, it will become increasingly inadequate for magnetic properties as well.

The remainder of the paper is organized as follows. In Sec. II, we introduce the Hamiltonian, and briefly outline some of its basic properties to facilitate the ensuing discussion. In Sec. III, we summarize the strategies used to solve the mean-field equations. Results for the 3D model are presented in Sec. IV; numerical results for the $\langle 100 \rangle$ - and the $\langle 111 \rangle$ -SDW are followed by a discussion where the pairing ansatz is first introduced and then used to help understand the numerical findings. The dimensional crossover results are then presented in Sec. V, followed again by a discussion based on insights from the pairing ansatz. We conclude in Sec. VI.

II. BACKGROUND

Given our goal to study both the 3D case and the crossover from 3D to 2D, it is most convenient to define the 3D Hubbard Hamiltonian as a stack of square-lattice planes. We will use $\mathbf{r} \equiv (x, y)$ to denote in-plane coordinates and z to label the planes. With this convention

the Hubbard Hamiltonian reads

$$\begin{aligned} \mathcal{H} = & -t \sum_{\langle \mathbf{r}\mathbf{r}' \rangle, z, \sigma} \left(c_{\mathbf{r}z\sigma}^\dagger c_{\mathbf{r}'z\sigma} + c_{\mathbf{r}'z\sigma}^\dagger c_{\mathbf{r}z\sigma} \right) \\ & -t_\perp \sum_{\mathbf{r}, \langle zz' \rangle, \sigma} \left(c_{\mathbf{r}z\sigma}^\dagger c_{\mathbf{r}z'\sigma} + c_{\mathbf{r}z'\sigma}^\dagger c_{\mathbf{r}z\sigma} \right) \\ & + U \sum_{\mathbf{r}, z} n_{\mathbf{r}z\uparrow} n_{\mathbf{r}z\downarrow}, \end{aligned} \quad (1)$$

where the operator $c_{\mathbf{r}z\sigma}^\dagger$ ($c_{\mathbf{r}z\sigma}$) creates (annihilates) a particle with spin σ ($\sigma = \uparrow, \downarrow$) at site (\mathbf{r}, z) and $n_{\mathbf{r}z\sigma}$ is the corresponding number operator. The hopping amplitude t is between nearest neighbor sites within a plane (denoted by $\langle \mathbf{r}\mathbf{r}' \rangle$ in the summation), t_\perp is the inter-plane hopping amplitude between nearest neighbor sites belonging to different planes (denoted by $\langle zz' \rangle$ in the summation), and $U > 0$ is the on-site interacting strength. Throughout this work, energy is quoted in units of t and we set $t = 1$. The Hamiltonian in Eq. (1) describes the 3D cubic Hubbard model when $t_\perp = 1$, the crossover between the square and cubic lattices when $0 < t_\perp < 1$ and a stack of decoupled 2D Hubbard planes when $t_\perp = 0$. Only unpolarized systems are considered, *i.e.*, the average densities of the two spin species are kept equal: $n_\uparrow = n_\downarrow$. The nature of the ground state is thus characterized by three parameters: the inter-plane hopping amplitude t_\perp , the on-site repulsion U and the doping (hole density)

$$h \equiv 1 - (n_\uparrow + n_\downarrow). \quad (2)$$

The particle-hole transformation, $c_{\mathbf{r}z\sigma}^\dagger \rightarrow (-1)^{x+y+z} c_{\mathbf{r}z\sigma}$, maps the $h < 0$ sector into the $h > 0$ one, regardless of the value of t_\perp or U , and we therefore confine our study to $h > 0$.

At half-filling, $h = 0$, the non-interacting Fermi surface is given by $-2(\cos k_x + \cos k_y + t_\perp \cos k_z) = 0$. Despite the lack of symmetry between the z - and the \mathbf{r} -directions for any $t_\perp \neq 1$, perfect nesting via $\mathbf{Q} \equiv (\pm\pi, \pm\pi, \pm\pi)$ remains throughout the whole surface, and causes an AFM instability for any $t_\perp \neq 0$ and arbitrary small U values. The evolution of the non-interacting half-filled Fermi surface as t_\perp varies is shown in Fig. 1. In the first column, representing the 2D limit, the Fermi surface has no dependence on k_z and any wave-vector of the form $(\pm\pi, \pm\pi, q)$ is perfectly nested on it. The arbitrariness of q is reflected in the complete lack of correlation between the \mathbf{r} -planes. The large nesting degeneracy is abruptly interrupted as soon as $t_\perp \neq 0$, and \mathbf{Q} remains the only nesting vector as the system evolves from the 2D limit toward 3D. The middle and bottom rows illustrate projections of the Fermi surface along the $\langle 100 \rangle$ - and $\langle 111 \rangle$ -directions; as we shall see in Sec.'s IV and V, the projected area of the Fermi surface plays a central role in determining the character of the SDW in the proximity of $h = 0$.

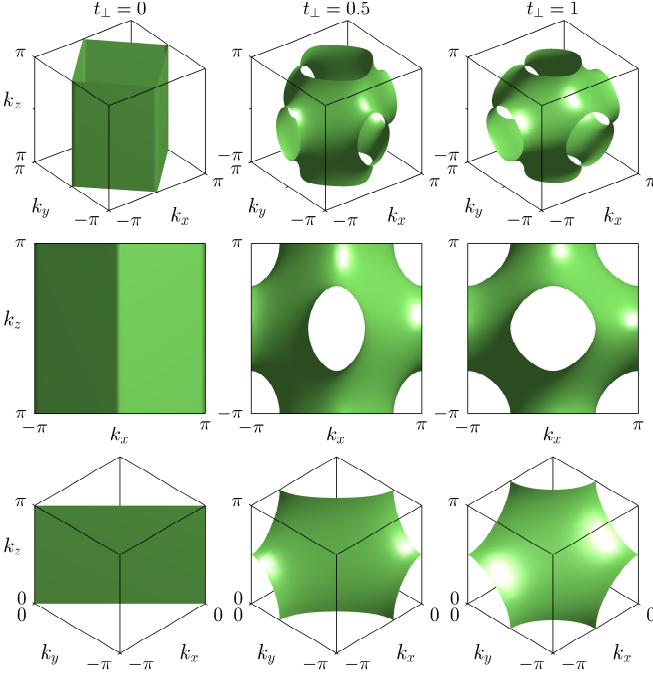


FIG. 1: (Color online) Non-interacting half-filled Fermi surface from different view angles: 3D (top), along $[010]$ (middle), along $[11\bar{1}]$ (bottom). From left to right, the columns are for $t_{\perp} = 0, 0.5$ and 1 , respectively. Note that only the surface in one octant is shown in the bottom row. Perfect nesting via $\mathbf{Q} = (\pm\pi, \pm\pi, \pm\pi)$ holds for any t_{\perp} at half-filling.

III. METHOD

The following mean-field formalism in real space is used in this work. A simulation cell of N sites is defined by three vectors, \mathbf{L}_1 , \mathbf{L}_2 and \mathbf{L}_3 , whose components are integers. Bloch states are then introduced as

$$c_{\beta}(\mathbf{k}) \propto \sum_{\mathbf{L}} c_{\beta+\mathbf{L}} \exp[i\mathbf{k} \cdot \mathbf{L}], \quad (3)$$

where \mathbf{L} are vectors of the form $\mathbf{L} = n_1\mathbf{L}_1 + n_2\mathbf{L}_2 + n_3\mathbf{L}_3$, \mathbf{k} is a reciprocal lattice vector that is free to vary within the first Brillouin zone (BZ) defined by the \mathbf{L}_i 's, and β labels sites inside the simulation cell. Using these states, the mean-field Hamiltonian can be decoupled into a sum of \mathbf{k} -dependent pieces, $H_0 = \sum_{\mathbf{k}} H_0(\mathbf{k})$, with each piece of the form

$$H_0(\mathbf{k}) = [\mathbf{c}_{\uparrow}^{\dagger} \mathbf{c}_{\downarrow}^{\dagger}] \begin{bmatrix} \mathbb{H}_{\uparrow}(\mathbf{k}) & \mathbb{S}^{-} \\ \mathbb{S}^{+} & \mathbb{H}_{\downarrow}(\mathbf{k} - \mathbf{G}) \end{bmatrix} [\mathbf{c}_{\uparrow} \mathbf{c}_{\downarrow}]^T, \quad (4)$$

where \mathbf{c}_{\uparrow} (\mathbf{c}_{\downarrow}) represents a row of operators $c_{\beta\uparrow}(\mathbf{k})$ ($c_{\beta\downarrow}(\mathbf{k} - \mathbf{G})$) with index β running through the N sites of the cell. A non-zero value of \mathbf{G} causes the spin densities at β and $\beta + \mathbf{L}_i$ to be related via a rotation by $\mathbf{G} \cdot \mathbf{L}_i$ around the z -axis. Charge and spin densities along z -direction obey periodic boundary conditions. \mathbb{H} and \mathbb{S}^{\pm}

are $N \times N$ matrices with elements

$$\begin{aligned} [\mathbb{H}_{\sigma}(\mathbf{k})]_{\beta\gamma} &= -t_{\beta\gamma}(\mathbf{k}) + \delta_{\beta\gamma}(UD_{\beta\sigma} - \mu), \\ [\mathbb{S}^{\pm}(\mathbf{k})]_{\beta\gamma} &= U\delta_{\beta\gamma}S_{\beta}^{\pm}, \end{aligned} \quad (5)$$

where $t_{\beta\gamma}(\mathbf{k}) = \sum_{\mathbf{L}} \exp(i\mathbf{k} \cdot \mathbf{L}) t_{\beta,\gamma+\mathbf{L}}$, and $D_{\beta\sigma}$, S_{β}^{\pm} and μ are determined by the requirement that the free energy $F = \langle H \rangle_0 - TS_0$ is a minimum for the targeted average density $n = n_{\uparrow} + n_{\downarrow}$. This amounts to the following SCF (gap) equations

$$\begin{aligned} D_{\beta,-\sigma} &= \frac{1}{(2\pi)^3} \int d\mathbf{k} \langle c_{\beta\sigma}^{\dagger}(\mathbf{k}) c_{\beta\sigma}(\mathbf{k}) \rangle_0 \\ S_{\beta}^{\pm} &= -\frac{1}{(2\pi)^3} \int d\mathbf{k} \langle c_{\beta,\pm\sigma}^{\dagger}(\mathbf{k}) c_{\beta,\mp\sigma}(\mathbf{k}) \rangle_0 \\ n &= \frac{1}{N(2\pi)^3} \sum_{\beta,\sigma} \int d\mathbf{k} \langle c_{\beta\sigma}^{\dagger}(\mathbf{k}) c_{\beta\sigma}(\mathbf{k}) \rangle. \end{aligned} \quad (6)$$

To locate the ground state we proceed with two complementary approaches. In the *first approach* we select the \mathbf{L}_i 's so that they span a large supercell containing $\mathcal{O}(5000)$ sites. A twisted boundary condition^{23,24} is applied, namely, using a single randomly selected k -point in place of the integrals in Eq. (6). The iterative process is started with various initial states, including random ones, and multiple annealing cycles are performed. In each cycle a random perturbation (whose strength can be controlled) is applied to a converged solution and the self-consistent process is repeated. Separate calculations for different k -points are done to check for consistency.

Once an understanding of the character of the ground state is gained, we use a *second approach* to target the specific family of states compatible with the results of the random search. For instance, suppose the random search finds a unidirectional SDW at small U values with wave-vector along the $\langle 100 \rangle$ -direction. We then choose a cluster of $\mathbf{L}_1 = (L, 0, 0)$, $\mathbf{L}_2 = (0, 1, 0)$ and $\mathbf{L}_3 = (0, 0, 1)$ with $\mathbf{G} = \pi((-1)^{L+2l}, 1, 1)$, where l is the number of oscillations of the order parameter, chosen to be an integer or half an integer. For a given set of the three parameters (t_{\perp}, U, h) , L is finely scanned (with L on the order of 50 and step size of 1) until the energy minimum is found. A large number of k -points is used (on the order of 100 in the two short directions and a few in the other) so that the character and properties of the targeted states can be accurately determined. This approach allows us to study different forms of SDW and long wavelength modes without increasing the computational cost.

In our study, we mix the two numerical approaches as needed and use them in complementary ways. For example, comparison of energies among several families of SDW is made with the second approach. To confirm the correctness of the ground state, the solutions are then checked against different initial states and annealing procedures using the first approach on a supercell commensurate with the optimal wavelength.

Various observables are computed to characterize the converged solutions. The local charge density ρ and the

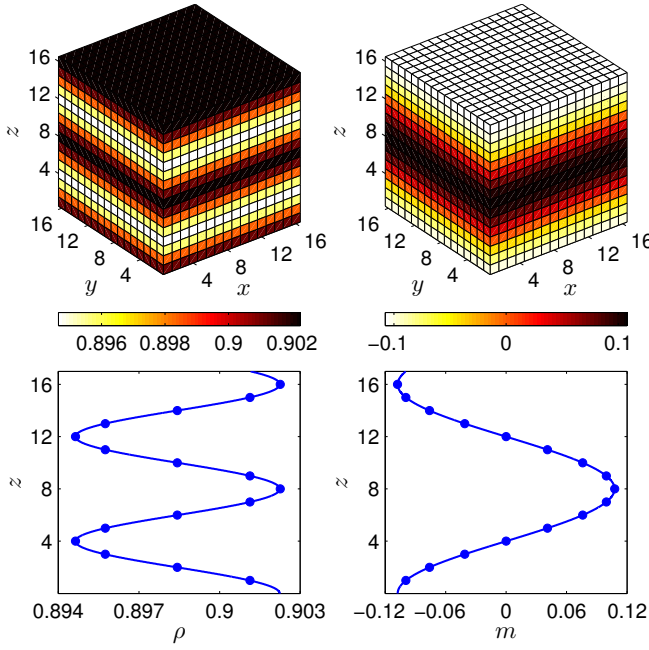


FIG. 2: (Color online) Charge density ρ (left) and order parameter m (right) of the solution for the 3D Hubbard model. Shown is a $16 \times 16 \times 16$ supercell, with $h = 13/128$ at $U = 2.5$. A linear wave is seen along the z -direction, with uniform AFM order in the xy -plane. The bottom panel shows a line cut along z -direction, with dots the actual data and the line a sinusoidal fit.

local order parameter, identified as the local staggered magnetization m , are defined as

$$\rho(\mathbf{R}) \equiv \langle n_{\mathbf{R}z\uparrow} \rangle + \langle n_{\mathbf{R}z\downarrow} \rangle, \quad (7)$$

$$m(\mathbf{R}) \equiv (-1)^{x+y+z} (\langle n_{\mathbf{R}z\uparrow} \rangle - \langle n_{\mathbf{R}z\downarrow} \rangle), \quad (8)$$

and used to characterize the state in real space (here $\mathbf{R} \equiv (\mathbf{r}, z)$). Since all the minimum energy solutions we find are unidirectional spin/charge density waves (SDW/CDW), it is natural to characterize them by their modulation wavelength along a relevant Cartesian axis, $\lambda_{\text{SDW/CDW}}$, defined by the leading component of the Fourier transform of ρ and m , respectively. The minima in the CDW are found to coincide with nodes in the SDW, thus $2\lambda_{\text{CDW}} = \lambda_{\text{SDW}}$. Below we will sometimes discuss our results in terms of a single wavelength $\lambda \equiv \lambda_{\text{CDW}}$, which can also be identified as the distance between two consecutive nodes of the order parameter. When we refer to the direction of the modulation, we will use $\langle 100 \rangle$ to denote symmetry-equivalent $[100]$ -directions, and similarly for $[110]$ and $[111]$.

To characterize the system in momentum space, we use the momentum distribution $n_{\mathbf{k}}$ and the momentum-resolved single-particle spectral function $A_{\mathbf{k}}(\omega)$, defined as

$$n_{\mathbf{k}\sigma} = \langle c_{\mathbf{k}\sigma}^\dagger c_{\mathbf{k}\sigma} \rangle, \quad (9)$$

$$A_{\mathbf{k}\sigma}(\omega) = \frac{1}{\pi} \text{Im} \langle c_{\mathbf{k}\sigma}(\omega - H + E_0 - i\eta)^{-1} c_{\mathbf{k}\sigma}^\dagger \rangle \quad (10)$$

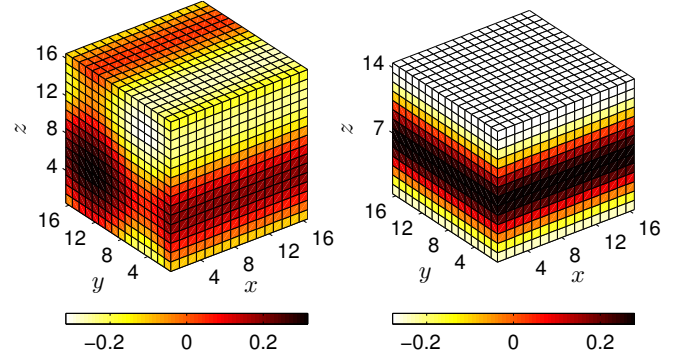


FIG. 3: (Color online) Spatial dependence of the order parameter m for $h = 13/128$, same as in Fig. 2, but with $U = 2.9$, on a $16 \times 16 \times 16$ supercell (left) and a $16 \times 16 \times 14$ supercell (right). Uniform AFM order in the xy -plane disappears for $L_z = 16$, but linear SDW along z -direction is seen again on the right with $L_z = 14$.

with $c_{\mathbf{k}\sigma} \propto \sum_{\mathbf{R}} \exp(-i\mathbf{k} \cdot \mathbf{R}) c_{\mathbf{R}\sigma}$. We use $n_{\mathbf{k}}$ to compare the converged mean-field solution with the pairing ansatz prediction and $A_{\mathbf{k}}$ to characterize the Fermi surface of the ordered phase.

IV. 3D RESULTS

A. SDW correlation in the $\langle 100 \rangle$ -direction

At half-filling, the existence of perfect nesting allows an AFM solution for any $U > 0$. Away from half-filling, perfect nesting ceases to exist and a finite critical value of the interaction is needed to cause the onset of order. The critical value U_c depends on h . Using the first approach described in Sec. III, we have determined that, just above U_c , the ground state of the system is an SDW with modulation along the $\langle 100 \rangle$ -direction. Figure 2 illustrates the spatial dependence of ρ and m in a $16 \times 16 \times 16$ supercell at $h = 13/128 \simeq 0.10$ and $U = 2.5$. The SDW is characterized by a single wave-vector and $\lambda_{\langle 100 \rangle} = 8$. The amplitude of the SDW is $\simeq 0.1$, roughly thirty times larger than that of the CDW. The simple form of the order found for $m(\mathbf{R})$ is indicative of the proximity of U to U_c . All of the observations above are consistent with the pairing model, as discussed below in Sec. IV C.

We next examine the evolution of $\lambda_{\langle 100 \rangle}$ as the interaction strength changes. Keeping h and the simulation cell unchanged and increasing U from 2.5 to 2.9, the random search returns the state displayed on the left panel of Fig. 3, which suggests that a more complicated type of order is seemingly settling in. We apply our second approach, using a dense k -point grid and a $1 \times 1 \times L$ simulation cell, to search for the optimal wavelength. We use large L (containing about 8 nodes in the cell) and vary its value until an energy minimum is found. Figure 4 shows the result of such minimization in terms of $\lambda_{\langle 100 \rangle}$; the minimum occurs when $\lambda_{\langle 100 \rangle} = 7$, indicating that the

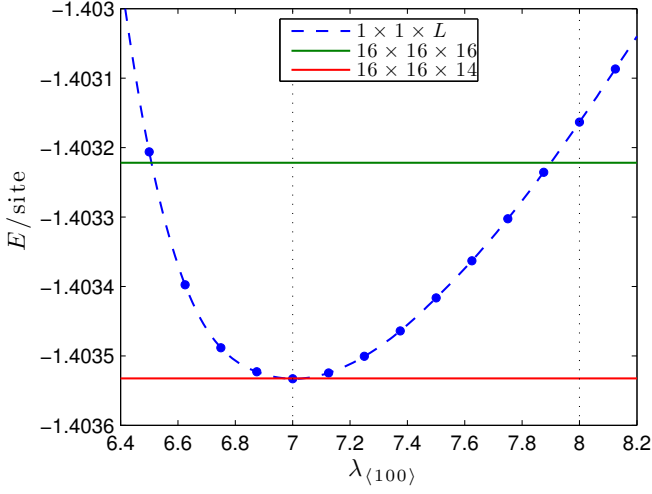


FIG. 4: (Color online) Energy of $\langle 100 \rangle$ -SDW (blue) vs. $\lambda_{\langle 100 \rangle}$ for a system of $h = 13/128$ and $U = 2.9$. Horizontal lines are the energies of the calculations shown in Fig. 3. The minimum of $\langle 100 \rangle$ -SDW is reached when $\lambda_{\langle 100 \rangle} = 7$. The state in the left panel of Fig. 3 leads to an energy higher than the minimum but lower than the energy with $\lambda_{\langle 100 \rangle} = 8$.

$16 \times 16 \times 16$ supercell is not commensurate with the wavelength of the minimum energy SDW state and that the pattern in the left panel of Fig. 3 is a result of frustration from an incommensurate supercell size. We next return to our first approach, and perform a new mean-field calculation, with *random* initial guess and annealing, on a $16 \times 16 \times 14$ supercell, a size which is commensurate with the wavelength of the minimum energy solution. And indeed we find the predicted state with $\lambda_{\langle 100 \rangle} = 7$ correctly reproduced (right panel in Fig. 3).

In Fig. 4, we report the energies of the two large supercell calculations of Fig. 3, to verify that the energy obtained in the $16 \times 16 \times 14$ supercell is correctly reproduced by the $1 \times 1 \times L$ cluster search with $\lambda_{\langle 100 \rangle} = 7$. The energy of the $16 \times 16 \times 16$ calculation, on the other hand, falls between those of $\lambda_{\langle 100 \rangle} = 7$ and 8. This gives a clear illustration of the characteristics of the two types of approaches. The supercell being incommensurate prevents the solution from collapsing onto the lowest energy SDW state of $\lambda_{\langle 100 \rangle} = 7$. The self-consistent solution in a large supercell then finds a different pattern that corresponds to the true ground state compatible with the imposed constraint. The energy of this state, computed by fixing the density and converging the value using a dense k -point mesh, is higher than the global minimum, but lower than that of the SDW state with an imposed wavelength $\lambda_{\langle 100 \rangle} = 8$.

We proceed to determine the exact dependence of the wavelengths on h and U by explicit solutions of the SCF equations in $1 \times 1 \times L$ clusters. Verifications of the results are done on large supercells whose sizes are commensurate with the wavelengths. Our results are summarized

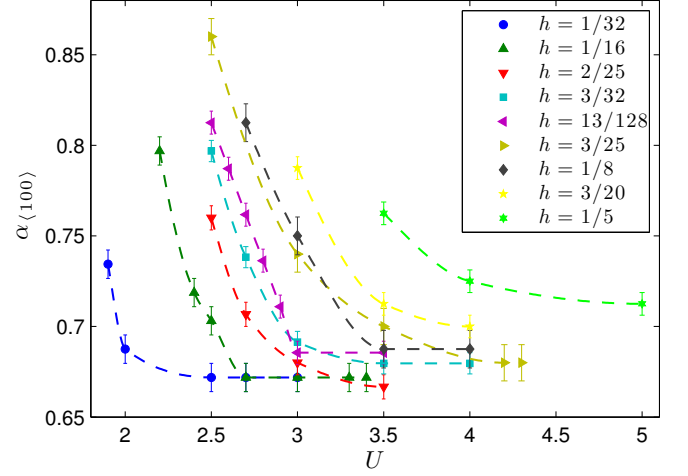


FIG. 5: (Color online) Characteristic wavelength as a function of U at various doping. $\alpha_{\langle 100 \rangle}$ gives the modulation wavelength, $\lambda_{\langle 100 \rangle}$, in units of $1/h$. As U is increased, the value of $\alpha_{\langle 100 \rangle}$ converges to approximately $2/3$ at small h (slightly larger at larger h).

in Fig. 5, with $\alpha_{\langle 100 \rangle}$ defined as

$$\alpha_{\langle 100 \rangle} = h\lambda_{\langle 100 \rangle}. \quad (11)$$

When the doping is small, the wavelength of the modulation is proportional to $1/h$, with $\alpha_{\langle 100 \rangle}$ almost independent of U and roughly equal to $2/3$. For larger h , $\alpha_{\langle 100 \rangle}$ converges to a slightly larger value. There is a general trend of an increase of $\alpha_{\langle 100 \rangle}$ as U approaches U_c from above. We will be able to rationalize these trends within the pairing model in Sec. IV C.

The evolution of the properties of the 3D SDW state with interaction U is similar to what is observed in 2D. Figure 6 shows 1D cuts of m and ρ in the z -direction, at $h = 0.05$ and U values such that $\alpha_{\langle 100 \rangle}$ has saturated to $\sim 2/3$. The figure illustrates the existence of U_c and the increase of the SDW and CDW amplitudes with U . It also shows the crossover from a regime where the order parameter has a smooth sinusoidal modulation and the holes are delocalized, to one where it is characterized by domain walls or stripes, with holes localized in the nodal regions.

There exists an important difference in the physics of the mean-field ground state of the 3D system and its 2D counterpart. While, in the latter, the system remains insulating when lightly doped, the 3D model immediately turns metallic. The difference is a consequence of the different behaviors of the modulating wavelength. In 2D, α is unity, independent of h and U , while in 3D it varies with parameters and has a non-integer value. To illustrate this in a simple case, consider a value of doping h such that λ ($\equiv \alpha/h$) is an integer. For such a system to be an insulator, the number of particles in a $1 \times 1 \times \lambda$ cell, $(1-h)\lambda = \lambda - \alpha$, will have to be an integer. However, because $\alpha \sim 2/3$ in the limit of small doping, the condition

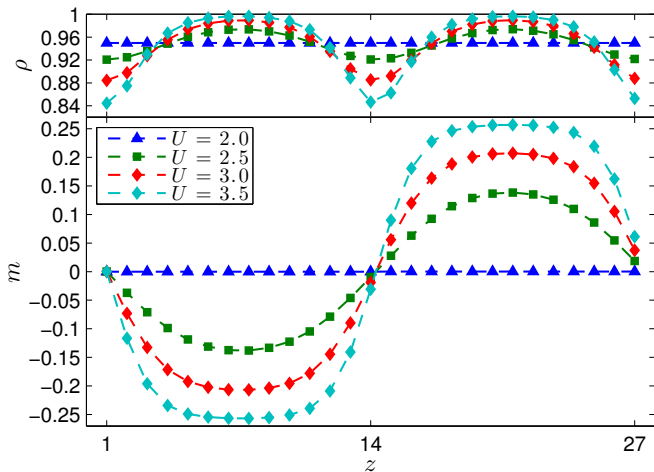


FIG. 6: (Color online) Charge density ρ (top) and order parameter m (bottom) vs. U . The system has doping $h = 0.05$. Each curve is a 1D cut along z -direction, the direction of the modulation. Beyond U_c , the $\langle 100 \rangle$ -SDW/CDW amplitudes increase with U and the solution evolves from a sinusoidal wave to domain walls. The CDW amplitude is much weaker than that of the SDW.

cannot be satisfied, and the system is necessarily metallic. A related way to see this is to consider the case of domain wall states, for example $U = 3.5$ in Fig. 6. Inside each domain wall (nodal region) are localized holes whose integrated (along the direction of the modulation) density is α . Thus the domain wall as a whole will act as a quasi-2D liquid of holes with non-integer density. We will discuss the corresponding momentum space signature in the next section.

B. SDW modulation along the $\langle 111 \rangle$ -direction

As shown above and further discussed in Sec. IV C, an orientation of the SDW other than $\langle 100 \rangle$ is not the solution in the proximity of U_c . However, when the interaction grows larger, other Fermi liquid instabilities become possible. This fact is clearly displayed when calculations on supercells commensurate with the optimal $\langle 100 \rangle$ -wavelength for a given U do not yield a state with $\langle 100 \rangle$ -SDW order. Figure 7 shows the occurrence of such a case in a calculation with $h = 1/8$ and $U = 5.0$, for which $\lambda_{\langle 100 \rangle} = 5.5$. The $16 \times 16 \times 22$ supercell should have precisely accommodated 4 nodal planes of the order parameter, but rather than doing so, the random search produces the lower energy solution shown in the left panel of the figure.

To search for the solution at higher U , we investigate unidirectional SDW's with modulation lying along either the $\langle 110 \rangle$ - or $\langle 111 \rangle$ -direction. An example is given in Fig. 8. The energies from constrained searches using the second approach are shown as a function of λ for a scan of U values. It is seen that, at and above $U = 4.5$, the

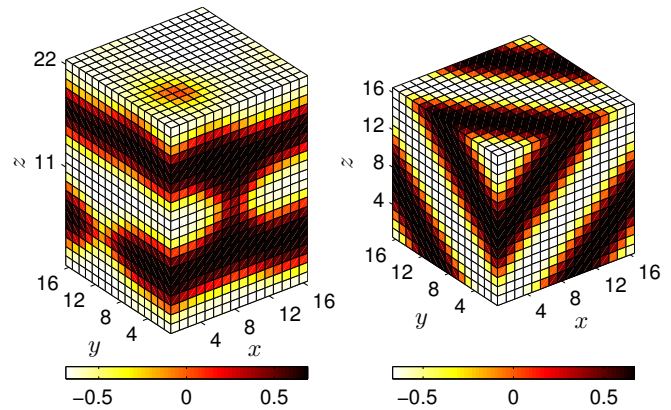


FIG. 7: (Color online) Order parameter m at $h = 1/8$ and $U = 5.0$ in a $16 \times 16 \times 22$ supercell (left) and a $16 \times 16 \times 16$ supercell (right). Though the supercell of $16 \times 16 \times 22$ is commensurate with the optimal $\langle 100 \rangle$ -wavelength, the random search produces a lower energy solution. The minimum energy solution is an SDW along the $\langle 111 \rangle$ -direction, which is correctly reproduced by a random search in a $16 \times 16 \times 16$ supercell as shown on the right.

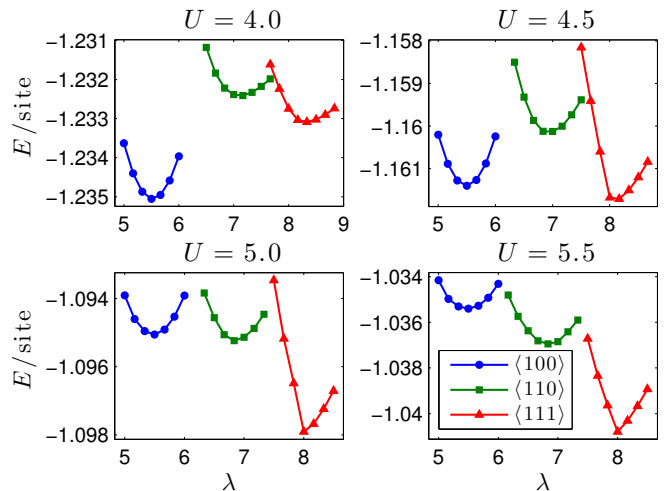


FIG. 8: (Color online) Energies per site of SDW in $\langle 100 \rangle$ -, $\langle 110 \rangle$ - and $\langle 111 \rangle$ -directions vs. λ for $h = 1/8$. At and above $U = 4.5$, the lowest energy state is modulated along the $\langle 111 \rangle$ - instead of $\langle 100 \rangle$ -direction.

lowest energy state is given by a $\langle 111 \rangle$ -SDW, instead of the $\langle 100 \rangle$ -order at lower U . For $U = 5$, the minimum energy solution is correctly reproduced by a random search in a $16 \times 16 \times 16$ supercell as shown in the right panel of Fig. 7. In our searches, $\langle 110 \rangle$ -direction SDW's are never found to be the global ground state.

By repeating the same procedure, we construct the equation of states for $U = 3$ and $U = 4$ contained in Fig. 9. At $U = 3$, there is no density regime where the $\langle 111 \rangle$ -SDW is the global ground state. In contrast, for $U = 4$, a discontinuous transition from $\langle 100 \rangle$ to $\langle 111 \rangle$ occurs around $n = 0.9$ with a small coexistence region.

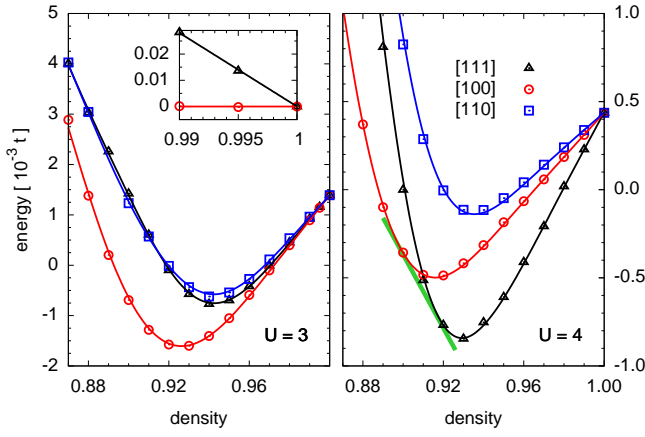


FIG. 9: (Color online) Ground-state energy per site from constrained search of $\langle 100 \rangle$ -, $\langle 110 \rangle$ - and $\langle 111 \rangle$ -SDW at $U = 3$ (left) and $U = 4$ (right). A linear common shift has been applied to the energies to highlight the convexity and the different trends. At $U = 3$, $\langle 111 \rangle$ -SDW is not the global ground state. (The inset shows a zoom of the energy difference between $\langle 111 \rangle$ - and $\langle 100 \rangle$ -SDW states as $n \rightarrow 1$.) At $U = 4$, the ground state is $\langle 111 \rangle$ -SDW for $n \gtrsim 0.92$.

In both cases the low-doping ground state is characterized by a linear energy-density dispersion. This bears two important consequences. First, contrary to what is observed using variational states with a uniform spiral order parameter²⁵, there is no sign of phase separation into a half-filled, AFM region and a hole-rich region. Second, the effective interaction between domain walls is short-ranged and their precise location in the hole-diluted limit is therefore irrelevant as long as they stay sufficiently far apart.

We find $\alpha_{\langle 111 \rangle} = 1$ at any density for which the $\langle 111 \rangle$ -SDW is the ground state. The $\langle 111 \rangle$ -SDW states are fully gapped, owing to the integer value of $\alpha_{\langle 111 \rangle}$, in contrast to the metallic behavior of the $\langle 100 \rangle$ states. Upon increase of U at a constant h , the structural transition is therefore always accompanied by a metal-to-insulator transition. We have verified, for selected cases, that random searches on larger supercells with sizes commensurate to the optimal wave-vector always return unidirectional SDW's with the same predicted wavelength and orientation. This provides a strong indication that the character of intermediate U instabilities remains that of a unidirectional SDW. Thus, as we increase U at constant density, the system is always expected to undergo a discontinuous transition from a $\langle 100 \rangle$ - to a $\langle 111 \rangle$ -SDW ground state.

C. A variational pairing ansatz

The pairing model is a variational ansatz that has proved extremely helpful in rationalizing the properties of SDW's in the mean-field treatment of the electron gas^{22,26} and the 2D Hubbard model²⁰. Similarly here,

the model helps to explain the numerical results and provides a simple conceptual framework that captures the essential physics of the SDW states in 3D and in the crossover regime discussed in the next section. We first summarize the formalism, and then apply it to the case of $\langle 100 \rangle$ -SDW at modest U , followed by the $\langle 111 \rangle$ -SDW.

At low U and small h , the pairing model is defined by spin-orbitals of the form

$$\phi_{\mathbf{k}\sigma}^\dagger = u_{\mathbf{k}} c_{\mathbf{k}\sigma}^\dagger + \sigma v_{\mathbf{k}} c_{\mathbf{k}+\mathbf{q}_{\mathbf{k}}\sigma}^\dagger. \quad (12)$$

The construction requires excitations to outside the Fermi sea. It is reminiscent of the ansatz used to construct the BCS pairing states for attractive interactions, except that here the tendency for small excitations is perhaps more “natural”, because of the repulsive interaction. A collection of spin pairs in orbitals given by Eq. (12) leads to a uniform charge density, $\rho(\mathbf{R}) = n$, and a spin density of the form

$$s(\mathbf{R}) = \frac{4}{N} \sum_{\mathbf{k} \in \mathcal{R}} a_{\mathbf{k}} \cos(\mathbf{q}_{\mathbf{k}} \cdot \mathbf{R}) \quad (13)$$

with $a_{\mathbf{k}} = u_{\mathbf{k}} v_{\mathbf{k}}$. The region \mathcal{R} over which \mathbf{k} is summed will be closely related to the non-interacting Fermi sea, and preserving the volume of $4\pi^3 n$, but will in general be slightly modified from the variational optimization, as we further discuss below. To ensure orthogonality amongst the spin-orbitals, $\mathbf{q}_{\mathbf{k}}$ must be such that $\mathbf{k} + \mathbf{q}_{\mathbf{k}} \notin \mathcal{R}$ and $\mathbf{k} + \mathbf{q}_{\mathbf{k}} \neq \mathbf{k}' + \mathbf{q}_{\mathbf{k}'}$. The corresponding potential energy per site is then given by

$$V = Un^2 - \frac{U}{4N} \sum_{\mathbf{R}} s^2(\mathbf{R}). \quad (14)$$

The potential energy lowering relative to the paramagnetic (PM) solution is thus:

$$\Delta V = -\frac{U}{N^2} \sum_{\mathbf{k}, \mathbf{k}' \in \mathcal{R}} a_{\mathbf{k}} a_{\mathbf{k}'} [\delta(\mathbf{q}_{\mathbf{k}} + \mathbf{q}_{\mathbf{k}'} + \mathbf{Q}) + \delta(\mathbf{q}_{\mathbf{k}} - \mathbf{q}_{\mathbf{k}'} + \mathbf{Q})], \quad (15)$$

where the Kronecker δ is intended as periodic on the reciprocal lattice, *i.e.*, modulo 2π in any direction.

Equation (15) makes it clear that the maximum reduction in V is achieved by having as many pairs as possible with $\mathbf{q}_{\mathbf{k}}$'s which are parallel or anti-parallel to each other. Noting that the vector \mathbf{Q} is perfectly nested when $h = 0$, let us consider the following explicit construction for \mathcal{R} : displace the half-filled Fermi surface in each octant of the first BZ by $\pm \Delta \mathbf{q}/2$, choosing the direction that shrinks the Fermi sea and with a length Δq such that the enclosed volume is reduced to $4\pi^3 n$. This construction is illustrated in the top panel in Fig. 10 for the case of the $\langle 100 \rangle$ -SDW (discussed next in Sec. IV C 1). The surface of \mathcal{R} can now anchor spin pairs with one common pairing vector, by making $u_{\mathbf{k}}$ less than 1 in a small layer immediately inside the surface of \mathcal{R} , and correspondingly $v_{\mathbf{k}} = \sqrt{1 - |u_{\mathbf{k}}|^2} > 0$.

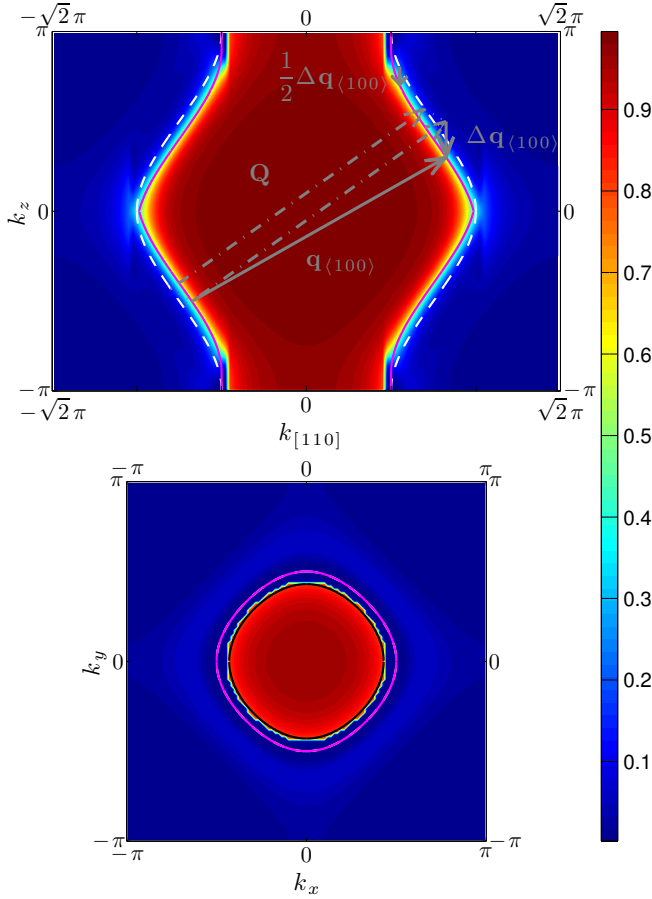


FIG. 10: (Color online) Illustration of the pairing model for the $\langle 100 \rangle$ -SDW state in 3D. The schematic diagram is drawn on the actual momentum distribution from the exact numerical solution for $h = 1/8$ and $U = 4.0$. The top panel shows the pairing construction on the contour plot of the $(1\bar{1}0)$ cut. The white dashed lines represent the half-filled surface, across which is the nesting vector \mathbf{Q} . The reconstructed surface, shown as magenta solid lines, is obtained by displacing the half-filled one along the z -direction by a distance $\Delta q_{\langle 100 \rangle}/2$, as given by Eq. (16). The nesting vector across the shifted surface, $\mathbf{q}_{\langle 100 \rangle}$, is shown by the long solid line with arrow. The bottom panel shows $n(\mathbf{k})$ of the $k_z = \pi$ plane. This is in a region where the Fermi surface survives the onset of order and where it differs more severely from the pairing construction. The actual Fermi surface, seen distinctly inside the reconstructed surface, differs little from the non-interacting Fermi surface (black solid line). $n_{\mathbf{k}}$ drops sharply, and no pairing is present in this region.

For small h , we can determine Δq directly from the construction:

$$\Delta q \int_S \hat{\mathbf{e}}_{\Delta \mathbf{q}} \cdot d\mathbf{S} = h \frac{\Omega_{\text{BZ}}}{2}, \quad (16)$$

where S is the half-filled surface, $\hat{\mathbf{e}}_{\Delta \mathbf{q}}$ is the direction of $\Delta \mathbf{q}$, and $\Omega_{\text{BZ}} = (2\pi)^3$ is the volume of the first BZ. Equation (16) implies a linear relationship between h and Δq and, using $\lambda = \pi/(\Delta \mathbf{q} \cdot \hat{\mathbf{e}})$, provides the following

estimate of α (Eq. (11))

$$\alpha_{\Delta \mathbf{q}} = \frac{1}{4\pi^2} \frac{1}{\hat{\mathbf{e}}_{\Delta \mathbf{q}} \cdot \hat{\mathbf{e}}} \int_S \hat{\mathbf{e}}_{\Delta \mathbf{q}} \cdot d\mathbf{S}. \quad (17)$$

where $\hat{\mathbf{e}}$ is a relevant Cartesian unit vector.

Different directions of $\Delta \mathbf{q}$ lead to different reconstructions of the non-interacting doped Fermi surface. The kinetic energy cost of the pairing ansatz can therefore be thought of as the combination of two contributions: the reconstruction energy due to using \mathcal{R} rather than the true non-interacting Fermi sea, and the kinetic energy change due to moving particles from \mathbf{k} (inside \mathcal{R}) to $\mathbf{k} + \mathbf{q}_{\mathbf{k}}$ (outside), *i.e.*, the non-zero $v_{\mathbf{k}}$'s. It is easy to see that, similar to 2D²⁰, at sufficiently large U the potential energy lowering will overtake the kinetic energy increase for the constructions discussed here. The correct state is determined by maximizing the gain in the potential energy from pairing (larger areas near the Fermi surface participating with parallel $\Delta \mathbf{q}$) while minimizing the kinetic energy cost.

The ansatz gives a clear picture for the onset of the instability. First, by its form, the model captures how the energetically costly CDW can be suppressed compared to the SDW. Second, it indicates that amongst different possible choices of $\mathbf{q}_{\mathbf{k}}$, the one involving only parallel and anti-parallel vectors are optimal. Third, the direction of $\pm \Delta \mathbf{q}$ must be such as to lead to the minimal possible reconstruction of the doped Fermi surface. These findings are in qualitative agreement with the numerical results obtained by the solution of the SCF equations: 1) the SDW is much stronger than the accompanying CDW, 2) the Fermi surface reconstructs in a way to enhance pairing and the SDW order tends to be unidirectional as a result, 3) more drastic reconstructions are only possible with larger U . Much quantitative information can be obtained with straightforward calculations using this model, as we discuss next for the $\langle 100 \rangle$ - and $\langle 111 \rangle$ -SDW states, respectively.

1. Analysis of the $\langle 100 \rangle$ -SDW

Among all directions, only a $\Delta \mathbf{q}$ along the $\langle 100 \rangle$ -direction causes the Fermi surface in each octant to shrink equally and this, it can be shown, leads to the minimum kinetic energy increase at small h . An SDW with $\langle 100 \rangle$ modulation is thus the lowest energy solution at low h and just above U_c , consistent with the results from explicit solutions of the SCF equations in Sec. IV A. We numerically calculate the projected area along the $\langle 100 \rangle$ -direction (shown in the right middle panel in Fig. 1) and obtain $\alpha_{\langle 100 \rangle} \simeq 0.63$, in very good agreement with the exact results from direct solutions shown in Fig. 5, where $\alpha_{\langle 100 \rangle} \simeq 0.66$. That the estimated value is slightly smaller is consistent with the presence of surviving Fermi surface inside the reconstructed doped Fermi surface as seen in Fig. 10.

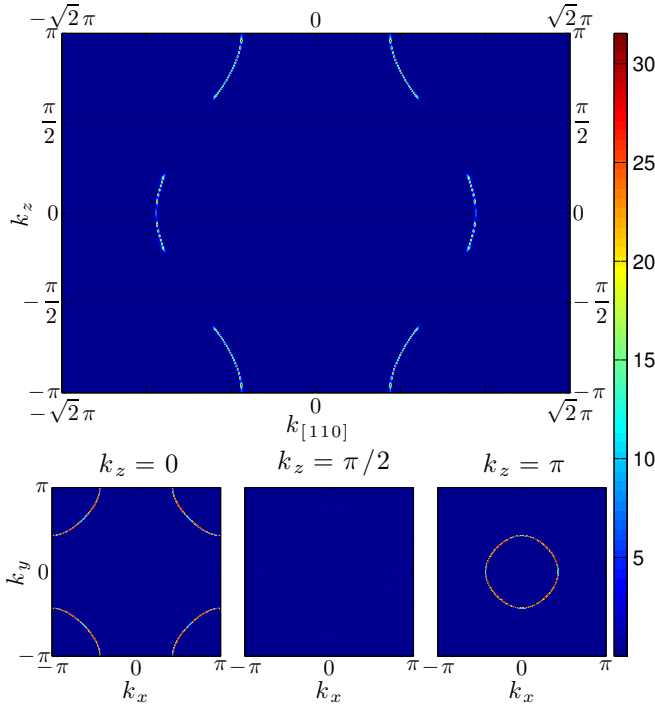


FIG. 11: (Color online) Contour plots of the single-particle spectral function evaluated at the Fermi energy; on the $(1\bar{1}0)$ cut (top) and on the $k_z = 0, \pi/2, \pi$ planes (bottom from left to right) for a system with $U = 2.7$ and $h = 1/8$. A large part of the Fermi surface survives, except for areas around the hot spots where it is most energetically favorable for pairing.

A direct comparison between the pairing model and the exact SCF solution can also be made in momentum space. We will identify the Fermi surface in the numerical solution from mean-field theory as the locus of points where $n_{\mathbf{k}\sigma} = 0.5$. Depending on the system and the value of U , the momentum distribution of the exact mean-field ground state can maintain a true Fermi surface, characterized by a discontinuity in $n_{\mathbf{k}}$, or have it smeared out by large pairing amplitudes (*i.e.*, $u_{\mathbf{k}}$ close to $1/\sqrt{2}$ near the boundary of \mathcal{R}). The two scenarios can occur in the same system at different \mathbf{k} values. The identification using $n_{\mathbf{k}\sigma} = 0.5$ is consistent with both.

Figure 10 shows, in particular, that the portion of the Fermi surface where pairing takes place is in very good agreement with the construction based on the pairing model, which indicates that the ansatz captures the dominant ingredient of the physics of the SDW state. The figure also provides a direct explanation for the survival of the Fermi surface around $k_z = \pi$ as it is there that the pairing construction shows large discrepancy with the true Fermi surface. This, in turn, implies that pairing in that region would be associated with too large a kinetic energy cost to be favorable. The absence of any gap from pairing at the Fermi surface in the $k_z = \pi$ plane is consistent with the picture discussed earlier of a quasi-2D liquid within each domain wall. These effects are amplified at smaller U 's as shown in Fig. 11, where a larger

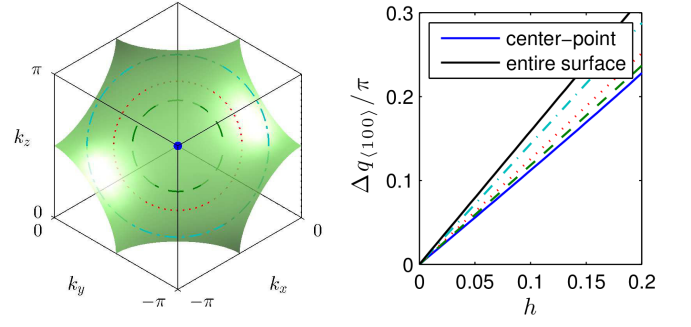


FIG. 12: (Color online) (a) Half-filled Fermi surface for the 3D Hubbard model in one of the octants (left) and (b) averaged $\Delta q_{(100)}$ over different areas vs. doping (right). The blue solid line in (b) is calculated at $(-\pi/2, -\pi/2, \pi/2)$, shown as the blue dot in (a). The dashed/dotted lines in (b) are averaged over varying areas as indicated by the circles with the same color/style in (a). The black line in (b) shows the averaged value over the entire surface, which leads to the estimate of $\alpha_{(100)} \sim 0.63$ discussed in the text.

part of the Fermi surface survives the onset of order; the parts that do not survive are in areas around the “hot spots” $\mathbf{k} \simeq (\pm\pi/2, \pm\pi/2, \pm\pi/2)$, where the pairing construction and the doped Fermi surface are most similar, and the change in $\frac{\partial \epsilon_{\mathbf{k}}}{\partial k_z}$ is at a minimum implying a closer proximity to a perfect common pairing vector.

These understandings allow quantitative explanations of all the features of the data on $\alpha_{(100)}$ shown in Fig. 5. For example, Fig. 12 shows that the distance along z -direction between the doped and half-filled Fermi surfaces is at a minimum around the hot spots. Given that such distance equals $\Delta q/2$ in the pairing construction, one finds that the local Δq value is smaller at the hot spots than when computed as the average distance over the entire surface. Hence, when only the hot spots are involved in pairing, a larger $\alpha_{(100)}$ results, as seen at lower values of U just above U_c . Obviously, the pairing reconstruction becomes increasingly accurate as h approaches 0. In this limit, one therefore finds the increasingly smaller U_c and the faster convergence (in U) to the saturated value of $\alpha_{(100)} \sim 2/3$ shown in Fig. 5.

2. Application to the $\langle 111 \rangle$ -SDW

By taking a displacement $\Delta \mathbf{q}$ along the $\langle 111 \rangle$ -direction, we can apply the pairing construction straightforwardly to the diagonal-modulated SDW. Analogously to the $\langle 100 \rangle$ case, Fig. 13 shows a remarkable agreement between the shifted half-filled surface and the calculated Fermi surface of the SDW. The two cuts in the figure clearly show broken cubic symmetry, where the Fermi surface in one pair of the octants is further away from the half-filled one so as to share the common modulation wave-vector $\Delta \mathbf{q}_{(111)}$ with the other three pairs. The $\langle 111 \rangle$ -SDW state offers, in this respect, a particularly

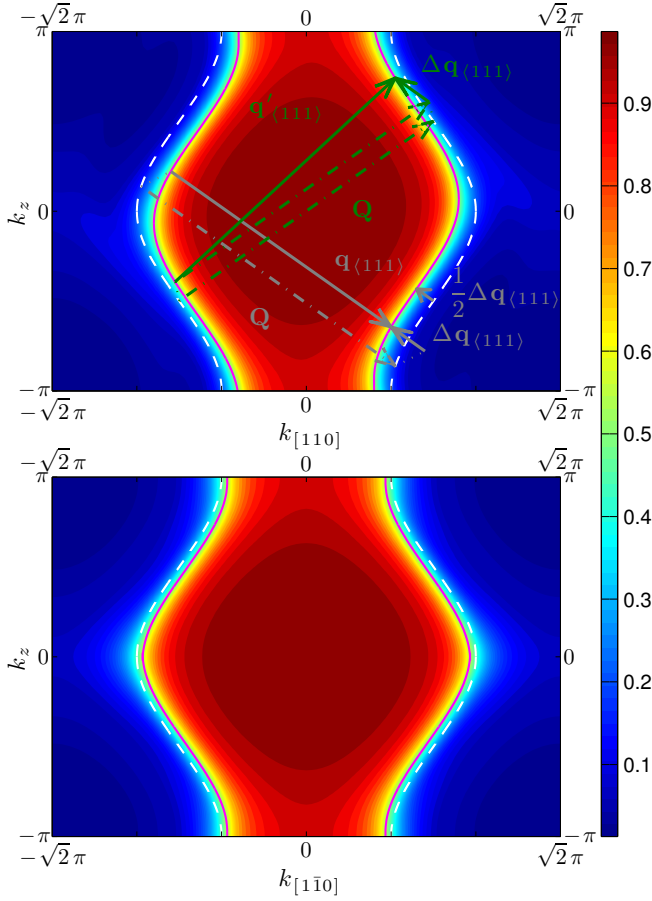


FIG. 13: (Color online) Schematic illustration of the pairing model for the $\langle 111 \rangle$ -SDW state, shown on the contour plots of the $\langle 1\bar{1}0 \rangle$ (top) and the $\langle 110 \rangle$ (bottom) cuts of $n_{\mathbf{k}\uparrow}$ for a system of $h = 1/8$ and $U = 5.0$. The white dashed lines are the half-filled surface, across which is the nesting vector \mathbf{Q} . The magenta solid lines show the pairing construction, obtained by shifting the half-filled surface along $[\bar{1}\bar{1}1]$ -direction by a distance of $\Delta q_{\langle 111 \rangle}/2$. In the upper panel, $\mathbf{q}_{\langle 111 \rangle}$ and $\mathbf{q}'_{\langle 111 \rangle}$ give two equivalent representations (differing by a reciprocal lattice vector) of the pairing vector across the reconstructed Fermi surface. Note the asymmetry between the two diagonal directions in the upper panel.

clear example where Fermi surface reconstruction can be observed. It also shows how an accurate experimental characterization of the momentum distribution in optical lattices can be used to characterize the band structure and pairing at the Fermi surface which, in turn, provides momentum space evidence on the real space character of the SDW.

Using Eq. (17) we have estimated the wavelength of the $\langle 111 \rangle$ -SDW, and found $\alpha_{\langle 111 \rangle} = 0.93$. The exact SCF calculations in Sec. IV B showed, instead, that $\alpha_{\langle 111 \rangle}$ is precisely pinned at 1 in a fairly large regime of U . This somewhat large discrepancy is a consequence of the natural tendency of the system to “lock” the integrated density of holes per nodal region to 1 whenever the topology of the non-interacting doped Fermi surface is such that

this is not energetically too costly. When doing so the system benefits from both pairing and band-insulating mechanisms to gap the entire Fermi surface and further lower the ground-state energy.

V. DIMENSIONAL CROSSOVER RESULTS

A. Results from full numerical HF solutions

The mean-field ground state of the doped 2D Hubbard model shares many similarities with its 3D counterpart. Just above U_c , the 2D system develops a sinusoidal SDW with a modulating wave along the $\langle 10 \rangle$ -direction and a much weaker accompanying CDW. As U is increased, the SDW increases its amplitude before the SDW state eventually changes into a collection of weakly interacting domain walls. Above a certain U , there is a discontinuous transition to a phase where the modulation is along the $\langle 11 \rangle$ -direction. The crossover from SDW to domain walls occurs before the $\langle 10 \rangle$ to $\langle 11 \rangle$ transition at small h , but after at larger h ²⁰. A peculiarity of the 2D case, due to the special topology of the 2D half-filled surface, is that $\alpha = 1$ and the system is an insulator regardless of doping, U or direction of the modulation wave-vector apart from a region close to U_c .

By controlling the distance between square lattice layers, optical lattice experiments allow the study of the evolution of the system as it crosses over from 2D to 3D. This situation is theoretically described by an increase of t_\perp in Hamiltonian (1) and the question, within mean-field theory, concerns the ensuing evolution of the ground-state properties. The pairing model and the arguments described in Sec. IV C remain valid in the crossover regime. We thus restrict our investigation to unidirectional SDW ground states, although we did use the first approach to carry out some searches, finding no additional structures. As in 3D, we verify that the SDW solution with minimum energy, identified using the second approach, can be obtained by the first approach in a large supercell that is commensurate with the optimal wavelengths, even when starting from random initial guesses. SDW in directions different from $\langle 100 \rangle$ or $\langle 111 \rangle$ are not found to be the global ground state for any value of t_\perp .

Results are summarized in the t_\perp - U mean-field phase diagram of Fig. 14. An overall increase in the critical U values is seen as doping increases, as a result of a greater deformation from the perfectly nested half-filled Fermi surface and the need for more excitations to achieve reconstruction of the Fermi surface for pairing. As before, numerical calculations focus on small doping ($h \leq 0.2$) and low to intermediate interactions ($U \leq 5.5$), where mean-field theory can be expected to be more accurate. Upon increase of U , and similarly to 3D, the system undergoes a first transition to a $\langle 100 \rangle$ -SDW state followed by a second, discontinuous transition to a $\langle 111 \rangle$ -SDW state. The absence of cubic symmetry away from $t_\perp = 1$ causes the modulation wave-vector for $\langle 100 \rangle$ -SDW to lie

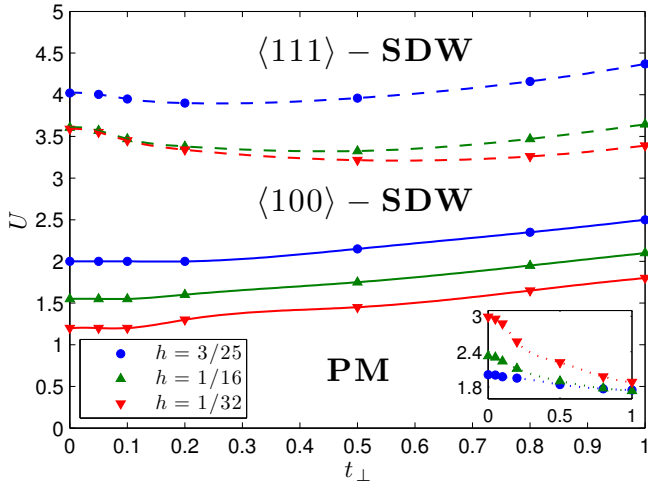


FIG. 14: (Color online) Mean-field phase diagram of the ground state in the crossover regime. Phase boundaries for several values of doping are indicated by symbols. The lines are to guide the eye. Solid lines separate the PM phase from the AFM phase, and dashed lines show transitions from $\langle 100 \rangle$ - to $\langle 111 \rangle$ -SDW. The inset plots the value of $U_{\langle 100 \rangle \rightarrow \langle 111 \rangle} / U_{\text{PM} \rightarrow \langle 100 \rangle}$.

in the xy -plane. This is because the elongation of the Fermi surface along z -direction (as illustrated in Fig. 1), meaning that $\Delta \mathbf{q}$ along z -direction leads to less surface area for pairing than along x - or y -directions. Wave-vectors along the $\langle 111 \rangle$ -direction continue, on the other hand, to remain equivalent under the symmetry operation of the tetragonal group.

The critical value of the interaction strength for the transition from the paramagnetic (PM) phase to $\langle 100 \rangle$ -SDW, $U_{\text{PM} \rightarrow \langle 100 \rangle}$, monotonically increases from 2D to 3D, due to the wider band width and smaller density of states at the Fermi energy for larger t_\perp . The transition values decrease to 0 when h approaches 0 as $U_c = 0$ for the half-filled system at any t_\perp . The critical U value for the transition from $\langle 100 \rangle$ - to $\langle 111 \rangle$ -SDW, $U_{\langle 100 \rangle \rightarrow \langle 111 \rangle}$, has a lower bound lying close to the $h = 1/32$ line in the figure, so that no $\langle 111 \rangle$ -SDW exists below $U \simeq 3$ regardless of the smallness of h and the value of t_\perp . In contrast with $U_{\text{PM} \rightarrow \langle 100 \rangle}$, $U_{\langle 100 \rangle \rightarrow \langle 111 \rangle}$ displays a non-monotonic behavior with t_\perp whose origin we will address in the next section.

The evolution of the modulation wavelength is summarized in Fig. 15 in terms of α as a function of t_\perp . Numerical results are obtained at U values around the transition line in Fig. 14, *e.g.*, just below $U_{\langle 100 \rangle \rightarrow \langle 111 \rangle}$ for $\langle 100 \rangle$. In a small window around $t_\perp = 0$, $\alpha_{\langle 100 \rangle}$ remains 1, as a direct consequence of the insulating character of the 2D solution. Apart from this region, there is a gradual decrease of $\alpha_{\langle 100 \rangle}$ with t_\perp (discussed further in the next section) and a weakening of the intensity of the order parameter (bottom panel of Fig. 15). As we have already remarked in the 3D results, the pinning of α at 1 in the $\langle 111 \rangle$ phase, and the corresponding insulating be-

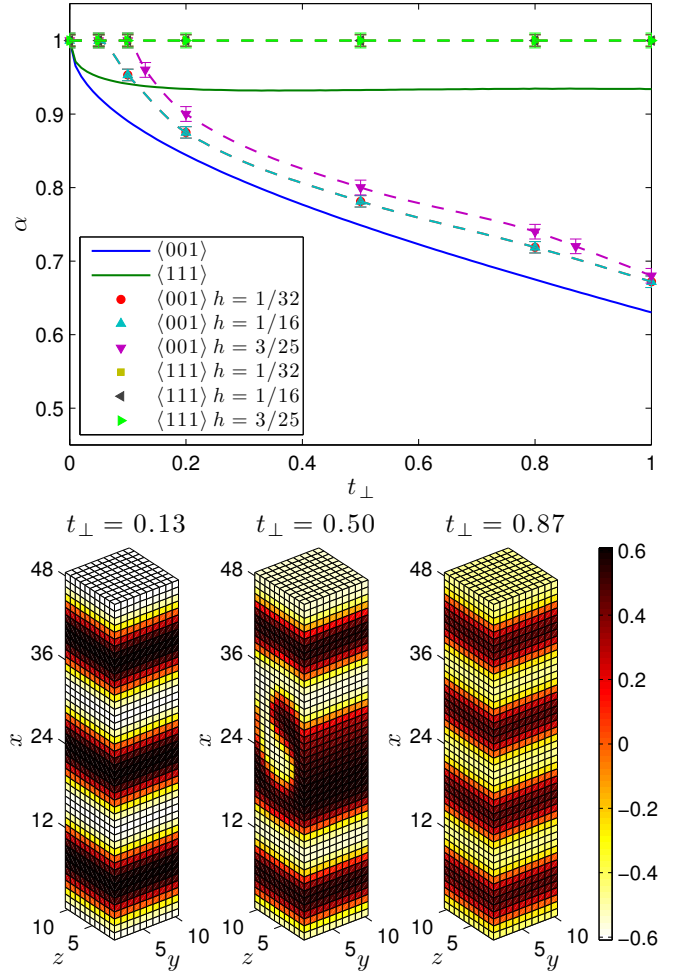


FIG. 15: (Color online) Top panel: dependence of the modulation wavelength on t_\perp . Numerical results for α (data points with error bars) at various dopings are compared with theoretical estimates (solid lines). Bottom panel: evolution of the order parameter on a $48 \times 10 \times 10$ supercell for $h = 3/25$, $U = 3.5$ as a function of t_\perp . As t_\perp increases, $\alpha_{\langle 100 \rangle}$ remains at 1 in a very small region close to 2D, before decreasing monotonically, while $\alpha_{\langle 111 \rangle}$ is locked at 1.

havior, are a result of a further stabilization of the ground state caused by coexisting magnetic and band-insulating effects.

B. Pairing model discussion

The dependence of α on t_\perp is captured by Eq. (17), as the projection of the Fermi surface $S(t_\perp)$ along $\Delta \mathbf{q}$. The middle and bottom rows of Fig. 1 show how the projected surfaces, along the $\langle 100 \rangle$ - and $\langle 111 \rangle$ -directions respectively, shrink as t_\perp is increased. Results from explicit calculations using Eq. (17) are shown as continuous lines in Fig. 15. They display a correct trend but a consistently underestimation of wavelengths. The quantitative disagreement is not surprising. The most significant

reason behind it is the tendency of α to be locked at 1, on which we have already commented and which apparently involves more global considerations than contained in the pairing model. The smaller discrepancy for the $\langle 100 \rangle$ -SDW outside the immediate vicinity of 2D, which increases for higher h , is due to the surviving FS that remains inside the reconstructed doped FS, as we have already remarked in the 3D results.

We next address the origin of the non-monotonic behavior of $U_{\langle 100 \rangle \rightarrow \langle 111 \rangle}$. This is the result of two competing factors. On the one hand, the increasing band width with dimensionality leads to an increase of U_c , as demonstrated in the monotonicity of $U_{\text{PM} \rightarrow \langle 100 \rangle}$. On the other hand, the geometrical properties of the Fermi surface are such that the angle between $\Delta \mathbf{q}_{\langle 111 \rangle}$ and the Fermi surface in some of the octants is small when t_\perp is small. This means that the displaced Fermi surfaces in those octants will remain close to the half-filling counterparts in the construction of \mathcal{R} (Sec. IV C). As a result, the other components of the Fermi surface must be displaced further to preserve total volume, causing a more uneven reconstruction which requires more excitations from the non-interacting Fermi sea, hence larger U_c . The 2D case offers an extreme example of this as it is characterized by a large fraction of the reconstructed doped surface remaining exactly pinned on the half-filled one²⁰. To separate this factor from that of the band width, we examine $U_{\langle 100 \rangle \rightarrow \langle 111 \rangle} / U_{\text{PM} \rightarrow \langle 100 \rangle}$, which is plotted in the inset of Fig. 14. A monotonic decrease is seen with t_\perp . Therefore, $U_{\langle 100 \rangle \rightarrow \langle 111 \rangle}$ first decreases and then increases as t_\perp goes from 0 to 1.

VI. SUMMARY AND DISCUSSION

This work addressed quantitative aspects of possible inhomogeneous magnetic phases of the 3D Hubbard model that emerge as the average density deviates from one particle per site. Because of the ease with which experiments are expected to be able to transition between the 2D and 3D regimes, we also studied the evolution of the inhomogeneous ground state as a function of the hybridization between parallel layers of square lattices. Within mean-field theory, we have shown that the leading instability of the PM ground state is an SDW with long wavelength modulation along the $\langle 100 \rangle$ -direction. No tendency toward phase separation was seen, even at small values of doping. The system remains metallic, regardless of the proximity to half-filling, because of a non-integer density of holes per wavelength of modulation. This density is largely determined by an entirely geometric property of the Fermi surface: its projected area along the direction of modulation. At larger U values, the

ground state continues to be a unidirectional SDW, but with $\langle 111 \rangle$ -orientation. This phase is insulating and characterized by a significant distortion of the momentum distribution. Such distortion leads, quite naturally, to the identification of a reconstructed Fermi surface whose observation in optical lattice experiments should be feasible.

We showed that much of these results can be understood by a simple variational ansatz with pairing orbitals formed by a linear combination of two plane waves. By placing a pair of up- and down-spin particles into a pair of such orbitals, an SDW is formed with constant charge density. Straightforward analysis of the energetics from this ansatz leads to quantitative predictions of the wavelength and nature of the SDW modulation which are verified by our direct numerical solutions of the SCF equations.

The true many-body ground state will modify the mean-field solutions in several ways. For example, quantum Monte Carlo calculations in periodic simulation cells will restore translational invariance, and the inhomogeneities seen here will be manifested in spin-spin correlations and such. A deeper issue is the possible existence of additional competing instabilities once a fuller treatment of quantum fluctuations is included. Certainly, the tendency for magnetic inhomogeneous order is exaggerated in mean-field theory, and a more accurate description of the many-body correlation at a certain U value tends to be given by the mean-field results at a significantly weaker U . However, as we have shown in 2D, mean-field theory appears to capture the correct basic picture of the magnetic correlations when compared to quantum Monte Carlo results^{19,20}. This indicates that the results in the present paper can provide a useful framework for understanding the magnetic correlations in 3D and in the crossover regime for weak to intermediate interaction strengths.

Apart from the obvious omissions inherent in the mean-field approximation, this study has not addressed the fact that experiments are performed in the presence of a confining potential. Nor have we addressed how the situation is modified by a finite magnetization. Generalization of the present approach to address such issues will be valuable, and technically straightforward.

Acknowledgments

The work was supported by NSF (DMR-1006217) and ARO (56693-PH). Computational support was provided by the Center for Piezoelectrics by Design. We thank R. Hulet, H. Krakauer, and E. Rossi for useful discussions.

¹ O. Morsch and M. Oberthaler, Rev. Mod. Phys. **78**, 179 (2006).

² M. Lewenstein, A. Sanpera, V. Ahufinger, B. Damski, A.

- Sen, and, U. Sen, *Adv. Phys.* **56:2**, 243 (2007).
- ³ I. Bloch, J. Dalibard, and W. Zwerger, *Rev. Mod. Phys.* **80**, 885 (2008).
 - ⁴ T. Esslinger, *Annu. Rev. Condens. Matter Phys.* **1**, 129 (2010).
 - ⁵ W. P. Su, *Phys. Rev. B* **37**, 9904 (1988).
 - ⁶ J. Zaanen and O. Gunnarsson, *Phys. Rev. B* **40**, 7391 (1989).
 - ⁷ H. J. Schulz, *J. Phys. France* **50**, 2833 (1989); *Phys. Rev. Lett.* **64**, 1445 (1990).
 - ⁸ M. Kato, K. Machida, H. Nakanishi, and M. Fujita, *J. Phys. Soc. Japan* **59** 1047 (1990).
 - ⁹ A. Singh and Z. Tešanović, *Phys. Rev. B* **41**, 614 (1990).
 - ¹⁰ M. Inui and P. B. Littlewood, *Phys. Rev. B* **44**, 4415 (1991).
 - ¹¹ J. Yang and W. P. Su, *Phys. Rev. B* **44**, 6838 (1991).
 - ¹² M. Ichimura, M. Fujita, and K. Nakao, *J. Phys. Soc. Japan* **61**, 2027 (1992).
 - ¹³ D. J. Scalapino, *J. Low. Temp. Phys.* **95**, 169 (1994).
 - ¹⁴ S. Zhang, J. Carlson, and J. E. Gubernatis, *Phys. Rev. Lett.* **78**, 4486 (1997).
 - ¹⁵ R. Zitzler, Th. Pruschke, and R. Bulla, *Eur. Phys. J. B* **27**, 473 (2002).
 - ¹⁶ T. A. Maier, M. Jarrell, T. C. Schulthess, P. R. C. Kent, and J. B. White *Phys. Rev. Lett.* **95**, 237001 (2005).
 - ¹⁷ M. Capone and G. Kotliar, *Phys. Rev. B* **74**, 054513 (2006).
 - ¹⁸ T. Aimi and M. Imada, *J. Phys. Soc. Japan* **76**, 113708 (2007).
 - ¹⁹ C.C. Chang and S. Zhang, *Phys. Rev. Lett.* **104**, 116402 (2010).
 - ²⁰ J. Xu, C.C. Chang, E. J. Walter, and S. Zhang, *J. Phys.: Condens. Matter* **23**, 505601 (2011).
 - ²¹ C. J. M. Mathy, D. A. Huse, and R. G. Hulet, *Phys. Rev. A* **86**, 023606 (2012).
 - ²² S. Zhang and D. M. Ceperley, *Phys. Rev. Lett.* **100**, 236404 (2008).
 - ²³ D. Poilblanc, *Phys. Rev. B* **44**, 9562 (1991).
 - ²⁴ C. Lin, F. H. Zong, and D. M. Ceperley, *Phys. Rev. E* **64**, 016702 (2001).
 - ²⁵ P. A. Igoshev, M. A. Timirgazin, A. A. Katanin, A. K. Arzhnikov, and V. Yu. Irkhin, *Phys. Rev. B* **81**, 094407 (2010).
 - ²⁶ A. W. Overhauser, *Phys. Rev.* **128**, 1437 (1962).